Chapter 2

METHODS

In the current chapter the experimental techniques used in this work are described, and specifically, the Laser Ray Tracing (LRT) technique. The contributions of the author of this thesis have been mainly in the processing software (sections 2.2.2.2.- and 2.2.2.3.-), as well as calibrations (section 2.3.-) of the LRT device. Specifically, in this chapter are presented: 1) the general principles of the technique and the optical implementation of LRT used in the lab to measure the aberrations; 2) the software developed to control the device, as well as the software to process the raw images in order to compute the aberrations and to estimate eye movements during the measurement; 3) Different calibrations carried out to get the system ready for measurements; 4) the general protocol followed in the measurement sessions. The first description of the new LRT device, was presented as part of a poster (Dorronsoro et al., 2003b), at the Spanish Optical Society (SEDO) annual meeting (2003), where C. Dorronsoro won a Young Investigator Award as first author of this work, and as a talk at the Spanish Physics Society meeting the same year. The authors of this work were: Carlos Dorronsoro, Elena García de la Cera, Lourdes Llorente, Sergio Barbero and Susana Marcos.

The contribution of the author was: 1) participation on the design and implementation of the device (assistance in placement and alignment of elements in the setup, in hardware connections and in the installation of drivers); 2) testing and debugging the control software, giving feedback from the measurements and suggesting possible improvements; 3) developing of a new software for computing ocular aberrations from the retinal images using some routines from the previous device; 4) automating the software to compute eye movements from the pupil images; 5) calibration of the setup. An statistician advised most of the statistics used in this chapter.

2.1.- MEASUREMENT OF OCULAR ABERRATIONS: THE LASER RAY TRACING TECHNIQUE.

As mentioned in Chapter 1, there are different techniques to measure ocular aberrations. Most of the experimental measurements of aberrations in this thesis were performed using Laser Ray Tracing (LRT) technique. This technique was chosen for its advantages versus other techniques such as Hartmann Shack (HS) (see Chapter 1): greater dynamic range, which allowed to measure highly aberrated eyes without complications (see Chapter 7), and flexibility in the configuration of the sampling pattern (see Chapter 5).

The LRT technique was first applied to measure ocular aberrations in human eyes in 1997 (Navarro and Losada, 1997, Molebny et al., 1997). A deeper description of the method can be found at Moreno-Barriuso's thesis (Moreno-Barriuso, 2000). This is a double pass technique, since light is delivered into the eye and the reflection from the retina is captured on a CCD camera (see Figure 2.1). In the first pass the pupil of the eye is sequentially sampled with laser pencils parallel to the optical axis. Each ray is deflected at a specific angle α depending on the slope of the wavefront at that particular point of the pupil plane (defined by the optical characteristics of the surfaces it goes through), and therefore will impact the retina at a specific point. In an aberration-free system, all rays superimpose on the same retinal location. However, when optical aberrations are present the rays hit the retina at different positions. In the second pass the light is reflected off the retina, exiting the eye through the whole pupil, and forming an aerial image of the double-pass (or rather one-and-a-half-pass (Navarro and Losada, 1995)) point spread function (PSF) on a plane conjugated with the retina, but displaced an angle α away from the reference (chief ray, entering the eye through the pupil centre). This angle α is proportional to the slope of the wavefront at the point where the incoming beam entered the eye. This image is collected by a high resolution cooled CCD camera. Although in this second pass the aberrations of the eye affect the PSF, its position relative to the reference is not affected (as long as the PSF is contained within the isoplanatic area of the retina). Therefore, the angles are preserved, and the ray (transverse) aberration can be computed from the distance between the position (centroid) of the aerial image corresponding to each pupil location, and that corresponding to the aerial image for the reference ray (chief ray). The sampled pupil size is defined by the diameter of the sampling pattern projected on the pupil, and therefore, can be controlled by software (as long as the eye pupil is at least of the programmed diameter).

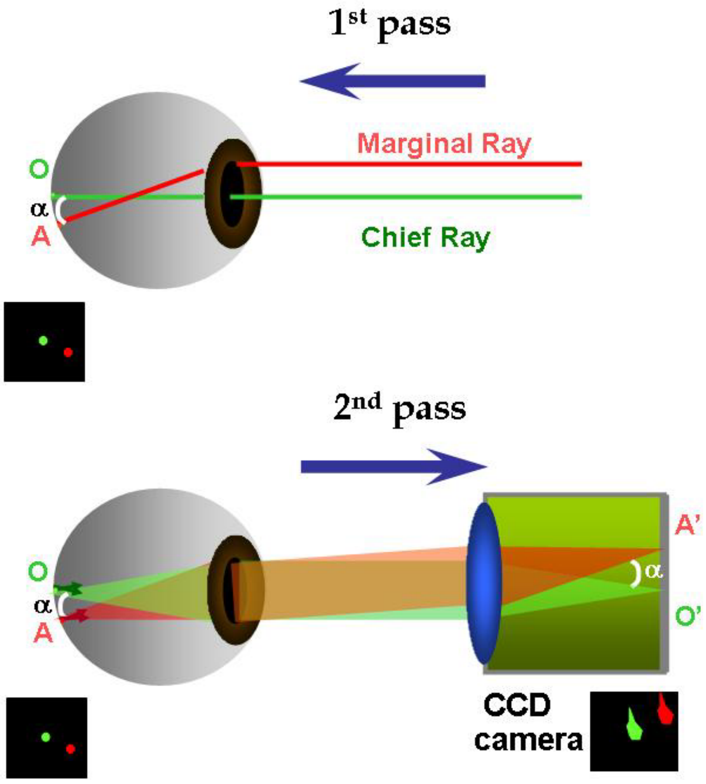

Figure 2.1. Laser Ray Tracing Technique.

In the 1st pass (top) rays are deviated due to the aberrations, in the 2nd pass (bottom) light reflected off the retina exits the eye through the whole pupil and is recorded by a CCD camera. O and A indicate the position where the chief and marginal rays strike the retina, respectively, separated an angle α. O′ and A′ indicate the position (centroids) of the aerial images corresponding to the chief and marginal rays, respectively, collected by the CCD camera. These are separated an angle α in the CCD. Modified from original diagram by S. Marcos and E. Moreno.

The wavefront phase is estimated by modal (Cubalchini, 1979) fitting of the directional derivatives of the wave aberration (transverse ray aberration) to the derivatives of the Zernike polynomials, using a standard least squares procedure. This approach has been chosen instead of zonal (Southwell, 1980) fitting due to the advantages previously mentioned (see Chapter 1, section 1.2.2) and because it is the standard in the visual optics field. A seventh-order Zernike polynomial expansion has been used in this thesis, unless indicated otehrwise. A representation of the Zernike functions can be seen in Figure 1.8, Chapter 1. In addition to Zernike polynomials, the Root Mean Square (RMS) wavefront error will also be used as a global metric for the optical quality. RMS is computed directly from the Zernike coefficients, using the following approximation:

$$RMS = \sqrt{\sum_{n,m} \left(Z_n^m\right)^2} \qquad (2.1),$$

where Z_n^m is the Zernike coefficient corresponding to the order n and frequency m. This approximation is considered valid, given that terms beyond 7th order can be considered negligible for human ocular aberrations(Porter et al., 2001, Castejon-Mochon et al., 2002, Thibos et al., 2002).

2.2.- THE LASER RAY TRACING DEVICE.

Two different LRT devices, both built at the Instituto de Óptica, Madrid (Spain), were used to measure ocular aberrations in this work. The first device (LRT1) was built by Esther Moreno during her doctorate research (Moreno-Barriuso, 2000, Moreno-Barriuso and Navarro, 2000, Moreno-Barriuso et al., 2001a, Moreno-Barriuso et al., 2001b) and was validated by comparison with other aberration measurement techniques, such as HS and the SRR (Moreno-Barriuso and Navarro, 2000, Moreno-Barriuso et al., 2001a). This device has been used in the work presented in Chapters 3, 4, and 7, and in part of Chapter 6. A diagram of this setup can be found in Chapters 3 and 4. The second device (LRT2), which will be briefly described in the next section, was developed during this work, and used in the work presented in Chapter 5 and part of Chapter 6. LRT2 incorporates some additional features especially advantageous for measurements in ametropic eyes (Dorronsoro et al., 2003b, Llorente et al., 2004a). The most important advantage of LRT2 over LRT1 is the possibility of correcting large amounts of spherical defocus continuously by means of a Badal system (see Section 2.3.5.- of this chapter) and the presence of a plane conjugate to the pupil plane (CPP), where trial lenses can be placed. Other improvements include: 1) the use of infrared (IR) light in addition to visible green light; 2) increase of the speed to less than 2 seconds for an entire typical run; 3) continuous display of pupil images during the measurement and simultaneous recording of the pupil and of retinal aerial images; 3) easy selection of the pupil sampling density and pattern by software; 4) fully automated control software; 5) it is more compact and lighter, what is especially advantageous to avoid misalignments of the optical components during transportation. The equivalence between both devices was verified, as will be shown in Section 2.3.8.- of this chapter, and was first reported in Llorente et al. (2004a). Measurements performed with both devices, unless differently indicated, followed the same protocols and were carried out under the same conditions (see section 2.4.-).

2.2.1.- EXPERIMENTAL SETUP

A schematic diagram of the LRT2 setup, as well as a photograph of the actual device are shown in Figure 2.2 A and B. The system consists of four channels; 1) Illumination channel, with two possible light sources (green 532 nm or IR 785nm laser diodes) focused on the XY scanner, and then collimated by the lens L3 in order to compose the desired sampling pattern on the pupil plane. 2) Retinal imaging channel, where the light reflected back from the retina is captured by the retinal CCD. 3) Pupil monitoring channel, where the pupil CCD captures the corresponding image of the eye's pupil, simultaneously with the retinal spots on the retinal CCD; 4) Fixation channel, where a target is displayed on a CRT monitor during the measurement. All channels share a Badal system, for compensation of defocus, formed by lenses L1 and L2 and mirrors M1, M2 and M3. P marks the position of a pupil conjugate planes, and R marks the position of retinal conjugate planes.

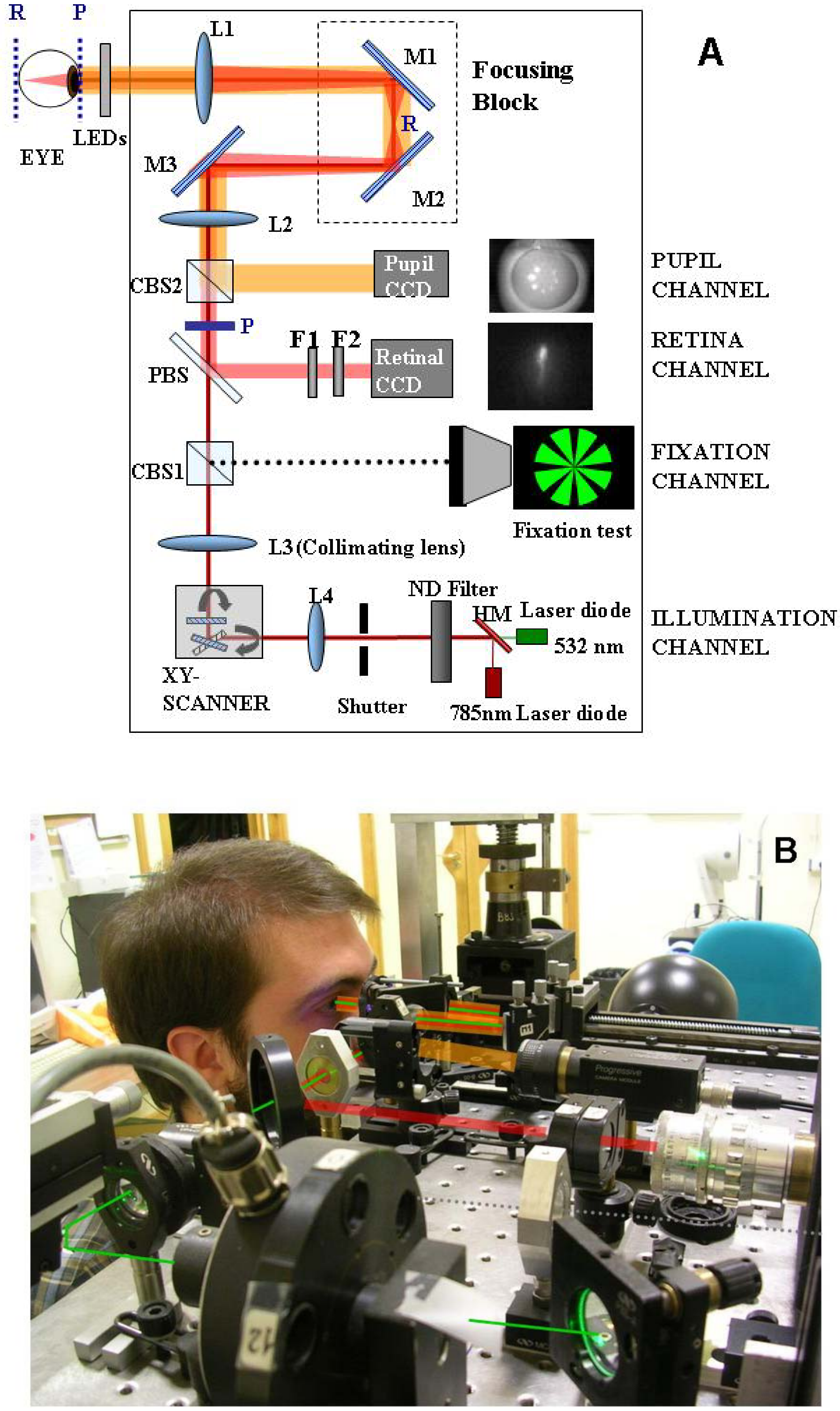

Figure 2.2. LRT2 setup described in the text.

A Schematic diagram of the device. L1 and L2 are 100-mm focal length achromatic doublets, and L3 and L4 are 50.8-mm focal length achromatic doublets, all with 25.4 mm diameters, M1, M2, and M3 are plane mirrors, HM is a hot mirror, CBS1 and CBS2 are cube beam splitters, PBS is a pellicle beam splitter, F1 and F2 are interferometric filters for 785 and 532 nm, respectively, and P and R are planes conjugate to the pupil and the retina, respectively. (B) Detail of the actual system during a measurement on a subject.

The light source can be selected between two diode lasers emitting in green (532 nm; Brimrose, Baltimore, USA) and IR wavelengths (785 nm; Schäfter + Kirchhoff, Hamburg, Germany). Prior to the systematic use of IR wavelength in the measurements, the equivalence of IR and green light in the measurement of ocular aberrations was confirmed (see Chapter 4). Both lasers were attenuated below safety limits using neutral density filters. The maximum permitted exposure (MPE) (ANSI, 2000, Delori et al., 2007) power thresholds for 532 nm and 785 nm (for 10 s exposure) were 576.2 µw and 54.µm respectively. At least three ND4 neutral density filters were used to attenuate the power down to 4.1 µw and 6.8 µw, and more filters where added when possible. Exposure times (about 1.5 seconds for a typical run with 37 samples) were controlled by an electronic shutter (Vincent Associates, Rochester NY, USA).

The XY scanner (mod.6210, Cambridge technologies, Lexington, USA), consists of two rotating mirrors that deflect the incoming unexpanded laser pencil in order to compose the sequential sampling pattern in combination with collimating lens L3 (f'=50.8 mm). Due to the distance between the two mirrors (~5 mm), some astigmatism is induced in the system (Navarro and Moreno-Barriuso, 1999), and therefore a trial lens attached to the collimating lens (+2.50 at 0^{o}) is used to correct this astigmatism (see Section 2.3.3.-). Lens L4 (f'= 50.8 mm) forms the image of the laser waist on the scanner in order to obtain the smallest sampling aperture on the pupil plane (~400 µm). The flexibility provided by the scanner to configure sampling patterns with different distributions and densities of the samples was essential for the study on sampling patterns reported in Chapter 5.

The light reflected off the retina is collected by a cooled highly sensitive CCD camera, conjugated to the eye retinal plane (retinal channel). The features of this camera are: 12 bits, 30 frames per second with 2x2 binning, 1024x1024 pixels, 14 µmx14 µm pixel size, 20% nominal maximum quantum efficiency (700 nm); model 1M15 by Dalsa, Waterloo, Canada. In addition to record aerial images, this camera can display them in real time. This allows to find objectively the best focus position while assessing the aerial image for a centred ray. During the measurement, the retinal camera is synchronised with the scanner and the pupil camera.

In the pupil channel a CCD continually monitors the pupil and records pupil images during the measurement. The features of this camera are: 8 bits, 60Hz (video), 646 (horizontal) x 485 (vertical) pixels, 7.4µmx7.4µm pixel size; model XC-55 by Sony Corp., Tokyo, Japan. Pupil real time images combined with the marks superimposed to the pupil image in the control program (see Figure 2.3), help to verify that everything is ready for the measurement: pupil located on the corresponding plane (pupil edges focused), alignment of the centre of the pupil and the optical system (centration cross) and suitability of the sampling pattern to the pupil diameter (small circumferences for samples entry locations and circumferences of different diameters to estimate pupil size). Pupil monitoring during the measurement allows to verify that no anomalies, such as blinking, large eye movements, tear problems, etc, occurred as well as to ensure the eye's stability. Five IR LEDs (peak wavelength 880±80 nm) arranged in a circular frame in front of the eye illuminate the pupil during the alignment (frontal-illumination). In addition, back-illumination is also possible when only the measurement light is used, and has proved to be very useful to visualise some features, such as crystalline lens opacities or tear film break up. Recorded images can also be used for passive eye-tracking (see Section 2.2.2.3.-), i.e. post-measurement correction on the pupil sampling coordinates when the eye moved during the measurement.

Recordings of a typical run can be seen at http://www.journalofvision.org/4/4/5/article.aspx#Movie1 (find also file movieLRT.mov attached to the electronic copy of the manuscript). In this file a video of the pupil (front-illuminated) as the entry beam scans discrete locations of the pupil is shown on the left. The ray entry position are marked with a circle. The corresponding retinal aerial images are shown on the right as the beam moves across the pupil. Figure 2.4 shows a frame of the movie.

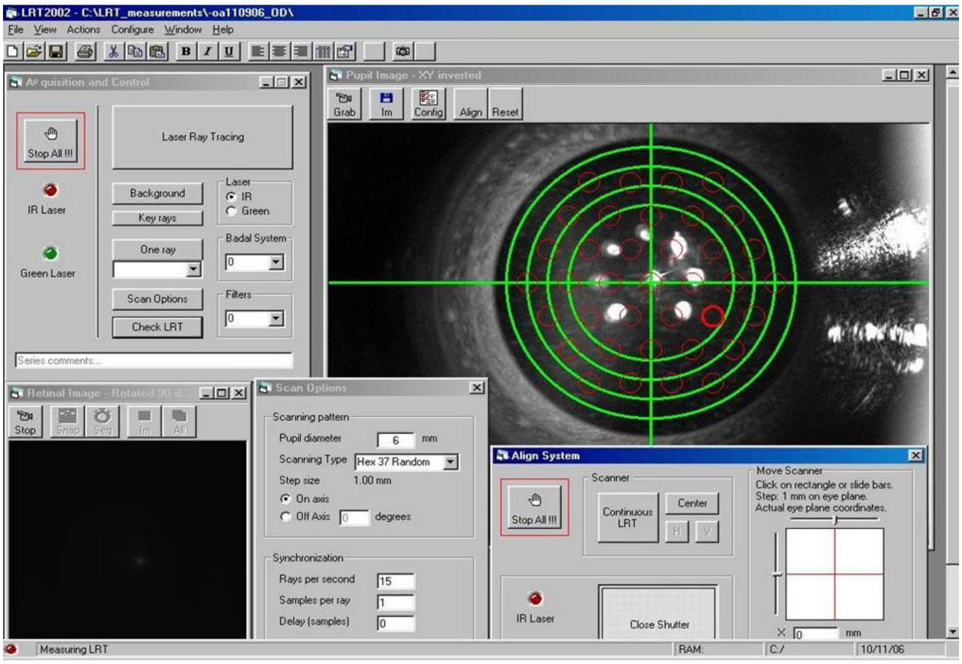
LRT2002 - C:\LRT_measurements\-oa110906_OD\

Laser: ● IR ○ Green
Badal System: 0
Filters: 0
Series comments...

Scanning pattern
Pupil diameter: 6 mm
Scanning Type: Hex 37 Random
Step size: 1.00 mm
● On axis
○ Off Axis: 0 degrees

Synchronization
Rays per second: 15
Samples per ray: 1
Delay (samples): 0

Move Scanner
Click on rectangle or slide bars.
Step: 1 mm on eye plane.
Actual eye plane coordinates.
X: 0 mm

Measuring LRT | RAM: | C:/ | 10/11/06

Figure 2.3 Snapshot of the control program developed by Carlos Dorronsoro for LRT2. Top right and bottom left are the pupil and retinal images, respectively

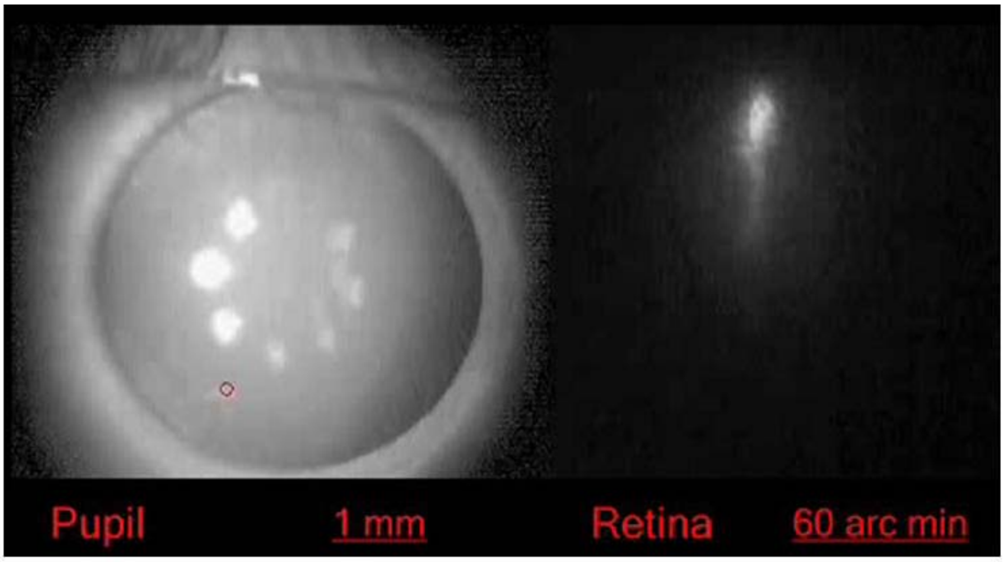

Figure 2.4. Frame of a movie showing a typical run with LRT2. The left image shows a frame of the (front-illuminated) pupil, with the entry point of the ray marked with a circle, and the right image shows the corresponding retinal aerial image. Both images belong to a frame of the movie that can be found at http://www.journalofvision.org/4/4/5/article.aspx#Movie1, showing recordings of a typical run with LRT2.

A 15 inches CRT monitor (Sony Corp., Tokyo, Japan) is used to project stimuli to help the subject to keep his/her eye fixed in optical axis direction of the system, and unaccommodated during the measurement. The fixation test, consisting of a green circle with black radial lines thickening towards the periphery (see fixation test in Figure 2.2 A), can be used to assess subjectively the refractive state of the subject's eye to be measured.

Finally, defocus correction in the system is carried out by a Badal system (Smith and Atchison, 1997), which allows to change the vergence of the rays (and hence defocus) without changing magnification, and therefore ensuring that the pupil magnification or the sampling density will not be affected by defocus correction. Our Badal system shares path with the different channels of the setup (see Figure 2.2 A), so that defocus is corrected in the illumination, imaging and fixation channels as well as the pupil monitoring channel. It is composed by two achromatic doublets (L1 & L2) of equal focal lengths (100 mm), that form an afocal system of magnification X1, and three flat mirrors: M3, which bends the optical path to obtain a more compact device, and M1 and M2, which can be moved as a block (Focusing Block) to change the optical path between the lenses, and consequently the dioptric correction (see Section 2.3.6.-). Moving the mirrors instead of the lenses has the advantage of not displacing the optical planes of the system. Spherical error corrections ranging from -5.50 D to +13 D can be induced with this system. Furthermore, easy access to pupil conjugate plane (P) allows to position trial lenses when a higher dioptric correction is needed.

2.2.2.- SOFTWARE

The software development was aimed at an intuitive and user-friendly, control program. The interface was written in visual basic (Microsoft Visual Basic; Microsoft Corp., USA), combined with Matlab (Matlab; Mathworks, Natik, MA) scripts. The data structure was organised so that data interchange between programs, such as control and processing software, was efficient, and tracking error sources was straightforward. The next subsections describe the control software, and processing software for retinal and pupil images software.

2.2.2.1.- System Control Software

New control software was created for the LRT2 setup by Carlos Dorronsoro. The aim was to make the measurements faster (less than 2 seconds compared to 4 seconds for the former LRT1, for 37 samples), and more flexible. The program also allowed to change easily the sampling pattern (scanned pupil diameter, sampling arrangement and density), what was very useful for the study comparing sampling patterns presented in Chapter 5. Figure 2.3 shows a snapshot of the control program. Pupil and retinal images can be visualised in real time, so that measurements could be discarded on-line, and a new series immediately be run. The software also facilitates alignment and calibration operations (see sections 2.3.2.- and 2.3.3.-.)

Particularly, the routine "Test LRT" allows to verify the correct delivery of the programmed pattern on the pupil. When this routine is activated, a series of circumferences indicating the nominal position of the samples and a centration cross appear superimposed to the pupil image (see pupil image frame in Figure 2.3). Simultaneously the shutter opens and the scanner starts to scan the programmed sampling pattern. A thicker circumference indicates the nominal position for the corresponding sample, i.e., the position where the laser spot should lie. When the central position is selected for the beam, alignment of the laser and optical axis the overlapping between the spot and the centration cross can be verified.

2.2.2.2.- *Processing Software for retinal images (ocular aberrations)*

The software to estimate the ocular aberrations from the set of aerial images was profoundly improved from its original LRT1 (Moreno-Barriuso, 2000) version in order to make the computation of aberrations easier, quicker, more robust and efficient, with better quality and traceability of errors or problems detection, and adapted to the new setup parameters and possibilities. The contribution of the author of this thesis in this software includes: collaboration in the design of the new data structure; writing of the new Matlab code; testing and debugging of the software; collaboration in the Visual Basic interface. Some specific improvements in the software include:

1) Calculation of those parameters necessary for the processing that depend on specific characteristics of the optoelectronics setup and inclusion of their values in the corresponding calibration data file;

2) Adaptation of the software to the new data structure defined by the control software: input data were read from the files created during the measurements, and structured result files were created for the output data;

3) Organisation of the program as a modular structure to allow for a Visual Basic interface, more efficient for the processing and more user-friendly;

4) Regarding image processing: possibility of choosing different processing parameters (thresholds, Zernike order to fit), as well as using default values; manual selection of the region of interest or of the images to exclude from the processing when necessary; possibility of undoing the last change; on-line visualisation of parameters significant for the processing such as maximum intensity of the images or spot diagram (joint plot of the centroids of the images already processed).

5) A graphic as well as numeric presentation of the results that allows to easily detect series that do not follow the common trend or do not have the same measurement conditions as the rest of the series of the same session. The results file also includes a worksheet where corneal aberrations are saved when available (see chapters 6 and 7), in order to summarise all the related results in one file.

A snapshot of the processing software interface is shown in Figure 2.5. Basically, raw images are processed (background subtraction, filters and masks application, thresholds setting, etc) in order to isolate each aerial image and localise the corresponding centroid. Then, the relative distance of each centroid to the central ray centroid is calculated (transverse aberration), and the wave aberration is then estimated by fitting the transverse aberration corresponding to each sampled point to the derivatives of the Zernike polynomials, using a least squares method (Cubalchini, 1979). The interface, as shown in Figure 2.5, allows the user to visualise the raw images, select the next processing to apply to the image and check the image appearance after processing has been applied, with the corresponding centroid position superimposed on the image. As previously mentioned, a joint plot with all the centroids positions (spot diagram) is also available. The program extracts the input data necessary for the wave aberration estimation from the corresponding excel file stored during the measurement, and saves the results in a new excel file in the corresponding project folder.

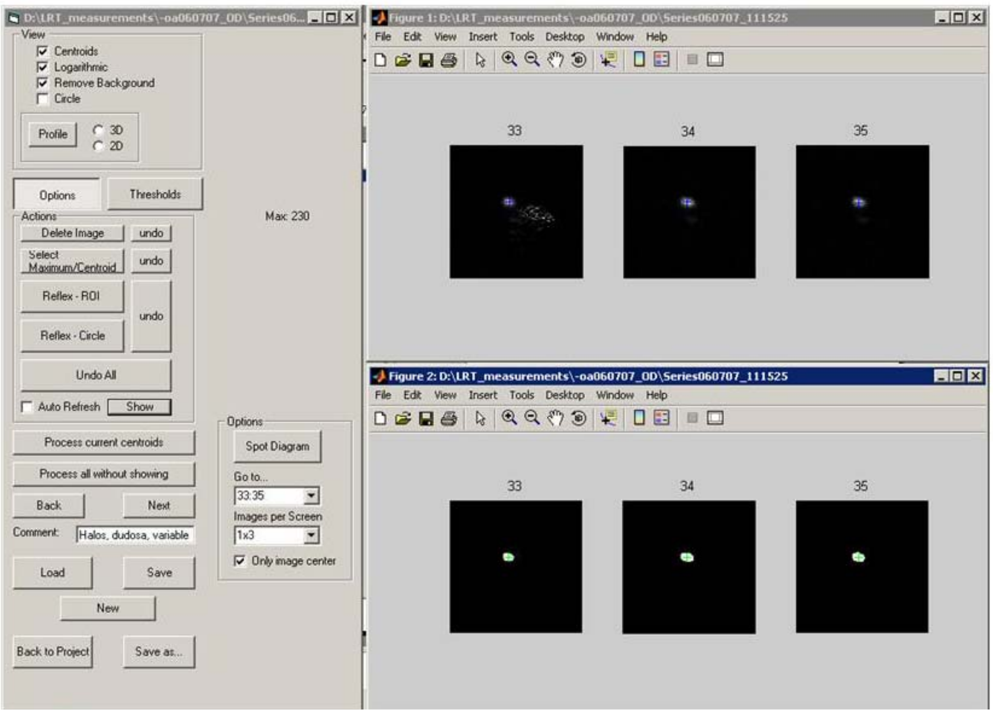

☑ Centroids
☑ Logarithmic
☑ Remove Background
☐ Circle
○ 3D
○ 2D
Max: 230
☐ Auto Refresh
Comment: Halos, dudosa, variable
Go to...: 33:35
Images per Screen: 1x3
☑ Only image center

Figure 2.5. Snapshot of the processing software interface showing some images before (top right) and after (top left) processing.

2.2.2.3.- *Processing software for pupil images (passive eye-tracking)*

A passive eye-tracker, based on the pupil images obtained during the measurements, was developed using image processing techniques to detect the pupil edge. This program made it possible to account for the influence of eye movements in the uncertainty of the measurement (see Chapter 5, Section 5.5.1).

As in the previous processing software, the parameters from the measurement necessary for this program are automatically read from the corresponding excel files, and the pupil images in the series are automatically opened (Figure 2.6 A). The program detects the edges within each image, and labels them (Figure 2.6 B). The edge corresponding to the pupil is selected by choosing those labelled areas which extension is larger than a set minimum. Then a binary image containing only the selected edge (Figure 2.6 C) is correlated with circumferences of different radius and thickness. The radius is chosen within a reasonable interval, considering the dimensions of the previously detected pupil edge, as well as realistic values for pupil radius, and the thickness is given by the desired tolerance. The greatest value across the maximum correlation values for each constructed circumference determines which circumference (radius) corresponds to the edge of the pupil, and its coordinates within the image indicate the position of the centre of the pupil (Figure 2.6 D). The circumference that yielded the best correlation is then used for the rest of the images of the series, as the changes in the dilated pupil radius are considered negligible within a series. Actual pupil coordinates (ray entry locations at the pupil, considering the pupil misalignment) are computed from the distance between the reference (optical axis of the system, where the pupil centre should be located during the measurement) and misaligned pupil centres (Figure 2.6 E). The output of the program includes the rays order, the nominal and actual ray pupil entry locations, and the radius and coordinates of the pupil centre (from the fitted circumference). Output figures include the outline (red dots) and centre (red cross) of the pupil circumference, as well as corresponding nominal (blue cross) and actual (red open circle) entry positions and the reference location (green cross) superimposed to each pupil image (Figure 2.6 E). Two summary images with joint plots are also produced: 1) nominal (blue crosses) and actual (red open circles) rays entry locations for all the images in the series (Figure 2.7 A), and 2) pupil centres computed for each images (blue Xs), with the reference (green cross) (Figure 2.7 B). The program takes about 255 seconds to process a series of 37 images. This speed was sufficient for our purposes, although further improvements of the program would result in a higher speed.

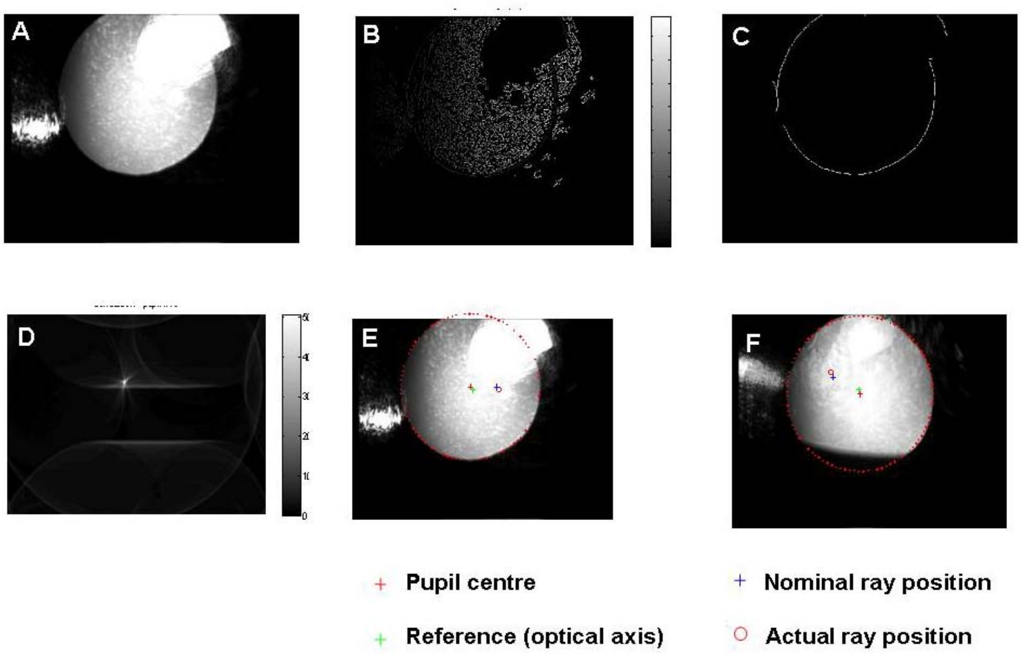

Figure 2.6. Illustration of the steps performed by the pupil processing software:. (A) input pupil image obtained from the control software; (B) same image labelled edges; (C) same image with only selected edges; (D) correlation values throughout the image for the selected construction circumference; (E) initial image with the resulting circumference outline (red dots) and centre (red cross) as well as corresponding nominal (blue cross) and actual ray (red open circle) entry locations.

This algorithm has proved to be robust for our back-illuminated images, even in the presence of strong reflections, or when the pupil was vignetted (see Figure 2.6 E) or partially occluded by the eyelid (see Figure 2.6 F). In the last case, it is important that the pupil is not occluded by the eyelid in the first image of the series. The algorithm was also tested for images of pseudophakic eyes, where the intraocular lens edge could be seen through the pupil. In this case, too many circles appeared in the image and the pupil could not be correctly identified. This algorithm may not work properly either for very elliptical (for example, in off-axis measurements) or asymmetric pupils. In the first case, using an ellipse instead of a circumference for the correlation would solve the problem. The second case is more complicated, as the pupil centre definition may not be very clear, to start from Since the algorithm was appropriate for the images to process, no work further along this line was made although, as explained, there is room for improvement.

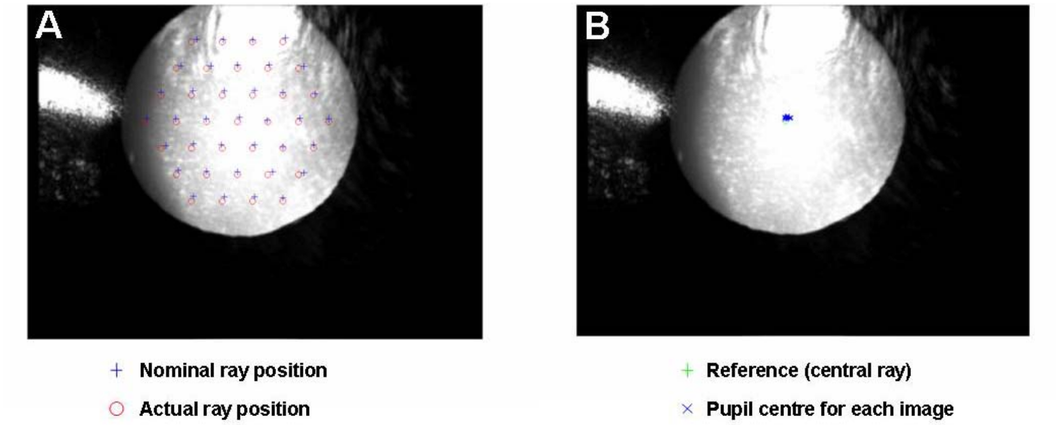

Figure 2.7. Example of output figures from the pupil processing showing: (A) joint plots of nominal (blue cross) and actual (red open circle) ray pupil entry locations, and (B) of the reference location and the pupil centre, across the pupil images corresponding to one series.

The analysis of the data provided by this programme allows to identify two different effects of the eye shift patterns: a shift similar to an offset that deviates the pupil from the reference position to another "balance" position (0 mm for x and 0.05mm for y, for the eye in Figure 2.7), and smaller shifts around this "balance" position during the measurement, where the pupil position changes slightly (0.05±0.06mm for x and 0.05±0.03mm for y for the eye in Figure 2.7). The first component will not only affect sequential techniques to measure eye aberrations, but any device that does not actively track the pupil and compensates for its shifts (active eye tracking). The actual pupil positions obtained from the programme can be used to compute the wave aberration and compare it with that obtained using the nominal positions. Figure 2.8 shows the wave aberration maps obtained for the eye in Figure 2.7, computed using the nominal coordinates (Figure 2.8 A), and the actual coordinates including only the second effect previously mentioned (Figure 2.8 B), and including both effects (Figure 2.8 C) as pupil sampling coordinates. Figure 2.8 D and F show the difference maps corresponding to the subtraction of A minus B and A minus C, respectively, both in the same scale. This algorithm was applied to the study reported in Chapter 5, where it was important to rule out the influence of the eye movements in the comparison across patterns.

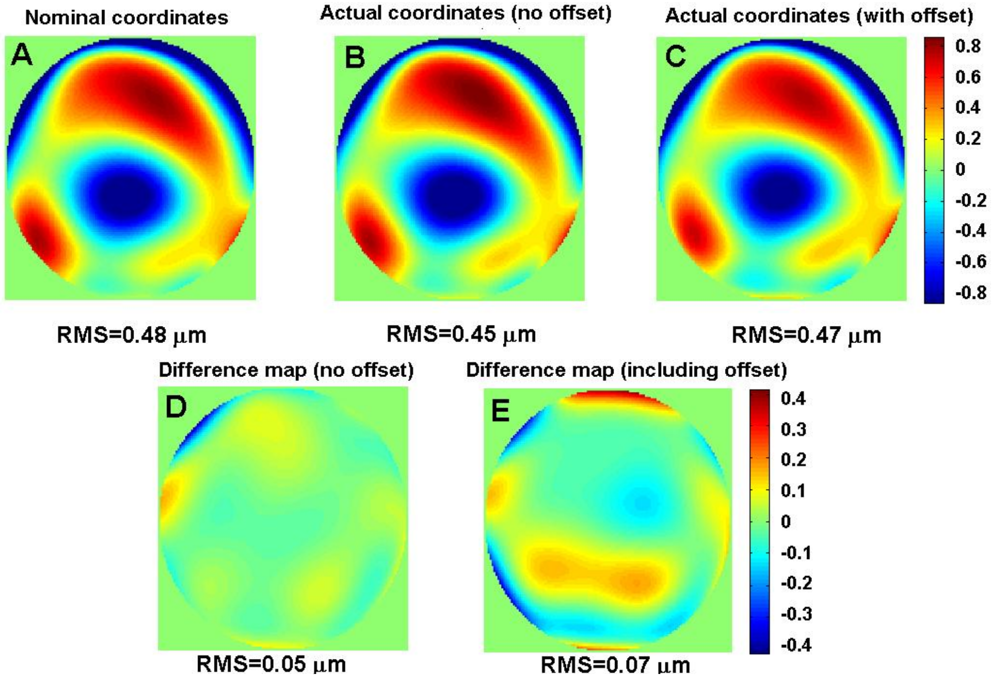

Figure 2.8. Wave aberration maps for the eye in figure 2.7 A computed using as pupil coordinates (A) the nominal entry pupil coordinates, (B) actual coordinates excluding offset effect , and (C) the actual coordinates including all eye movements effects. (D) and (F) show the difference maps (A) minus (B) and (A) minus (C), respectively, both represented in the same scale. The colour –bars unit is microns.

2.3.- SYSTEM CALIBRATION

2.3.1.- RETINAL CAMERA

Calibration of the equivalence between pixels and angles in the retinal camera images was achieved as follows. For this purpose, a metal calliper was placed at a plane conjugate to the sensor of the retinal camera, i.e., at the focus of the lens L2 (see Figure 2.2 A), and recorded the corresponding image with the CCD camera, illuminating the calliper with a lamp (see Figure 2.9A). In the recorded image (see Figure 2.9 B), the notches corresponding to a separation of 1 mm can be distinguished as lighter than the background. Matlab was used to process the image and determine the distance between notches in pixels. First the image was rotated until the notches were parallel to the vertical arrays of pixels of the image. Then, the edges of the image were detected, obtaining a binary image, and discarded those edges smaller than a set threshold to eliminate noise. Next, a region of interest was detected within the image (see Figure 2.9 C), which included the six notches on the right side. The position of the edges of the notches in this image were found, and the distance between the left edges of the first and last (6th) notches in the image computed. This distance was divided by 5 (number of separations between the notches) to find the distance separating the notches from each other. The result, averaged across the 89 rows of the image, was 27.0 pixels, and the standard deviation (std) was 0.8 pixels. This process was repeated for the right edges of the same notches, obtaining a value of 27.1 pixels with a std of 0.2 pixels. As a last verification, the distances between the centres of each notch were computed, obtaining an average of 27 pixels (std=1 pixel) across the 445 values (6 notches * 89 rows).

From Figure 2.9 A, α = arctan (1/100)=0.5729° = 34.38 arc min=0.01 rad. Therefore 1mm (27 pixels) subtends 34.37 arc min , and 1 pixel subtends 1.27 arc min. Consequently, since 1mm=27 pixels subtends 0.01 rad, then 1 rad = 27/0.01=2700 pixels, and hence 1 pixel subtends 0.37 mrad[1]. This value is used in the processing program to compute transverse ray aberration from the deviations of the spots in the CCD.

---

[1] According to the manufacturer (Newport) the tolerance in the focal length of the lens L2, is ±2% at 589 nm. This implies an error of ±0.0002 rad (0.69 arc min) in α, and therefore an error of ±0.007 mrad in the angle subtended by 1 pixel, i.e., ±2% of the error in α. The effect of this error in the estimates of the RMS wavefront error is ± 2%.

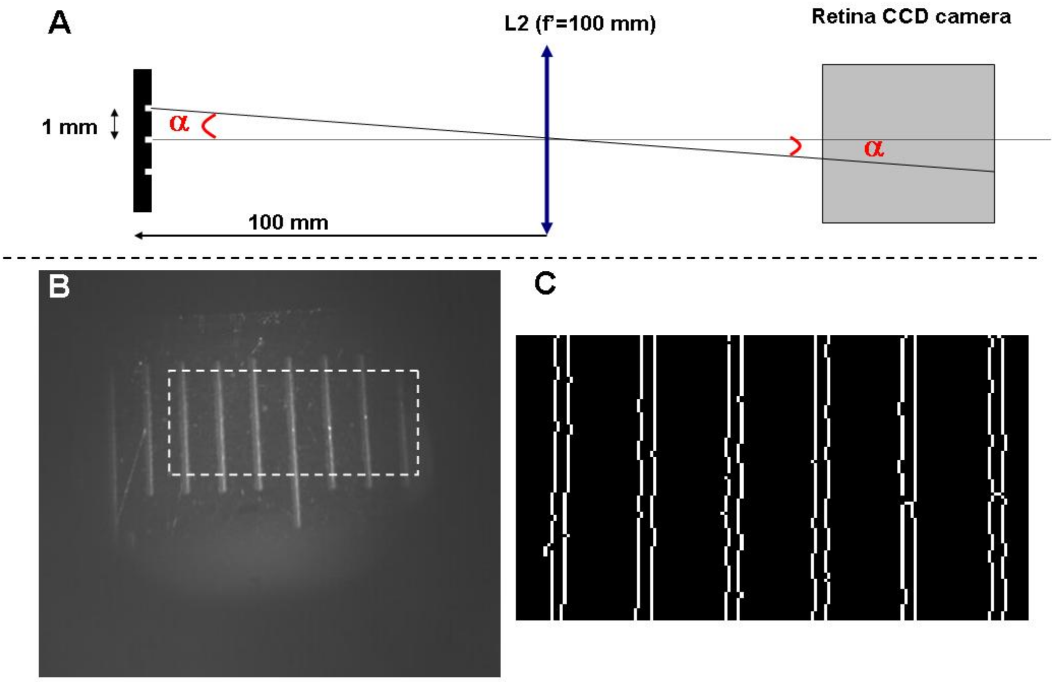

Figure 2.9. Retinal Camera Calibration: (A) Schematic diagram of the retinal camera calibration image acquisition. (B) Calibration image obtained; the lighter lines (corresponding to the notches of a calliper) are separated 1 mm. (C) Binary image showing the calliper notches edges of the region of interest delimited by the rectangle on image B, after rotation.

2.3.2.- PUPIL CAMERA

The pupil camera had several roles in the setup. It is used to ensure alignment of the eye pupil with the optical axis of the system, using the centration cross shown in Figure 2.3 as a reference. It can also be used to visualise the sampling pattern superimposed to the pupil, as well as to assess distances, such as the pupil diameter or pupil misalignment. Therefore, a) alignment between the centration cross (see section 2.2.2.1.-) and the optical axis must be ensured, by introducing the necessary offset, as the centre of the CCD might not coincide with the optical axis of the system and b) the scale of the camera must be calibrated so that distances and sizes can be accurately measured in the pupil images, or assessed in real time during the aberrations measurement session.

(a) Offset

Superimposition between the centration cross displayed on the pupil image shown by the control software (Figure 2.3) and the optical axis of the system was ensured by placing a paper screen at the pupil plane (plane where the subject's eye pupil is placed for the measurement), with the shutter open, and the scanner in the "centred" position, i.e., the measurement laser beam was co-aligned with the optical axis of the system. Under these conditions, the diffuse reflection of the laser (spot) was displayed on the pupil camera screen next (misaligned) or superimposed (aligned) to the centration cross. The cross was displaced by introducing new offset values for x and y directions in the calibration file, until overlapping the spot.

(b) Scale (equivalence between pixels and millimetres)

As mentioned above, the equivalence between pixels and millimetres on the pupil plane for the pupil camera was needed to measure distances in the pupil images. To determine this value, a graph paper screen was placed at the pupil plane so that the graph paper lines appeared as sharp as possible on the pupil camera, and captured the image under ambient light illumination. This image can be seen in Figure 2.10 A. The same procedure used for the retinal camera calibration to detect the edges of the squares could not be followed because the images were too noisy to detect the edges accurately. A different procedure was used instead. After rotating the image (-2.2º) so that the lines coincided as much as possible with rows and columns of the image matrix, the intensity values of the image were added up across rows to obtain the profile shown in Figure 2.10 B, and then the local minima were found (with an accuracy of one pixel). The most abrupt minima (indicated by crosses) correspond to the black lines of the grid, the wider of which corresponds to the wider line. Two minima (indicated with open circles in the figure) were selected and the distance between both points was computed and divided by the number of lines (millimetres) existing between them The value obtained was 43 pixels/mm. The procedure was repeated adding up the columns instead of rows and the same value was obtained, as expected, since the pixels of the camera are square.

2.3.3.- ASTIGMATISM CORRECTION AND SCANNER CALIBRATION.

In the absence of aberrations, a motionless spot was expected to appear at the focal point of L2 (see section 2.1.-) with the scanner on. However, a vertical line was scanned by the laser instead, indicating that some astigmatism was present in the system. As previously mentioned in section 2.2.1.-, some astigmatism was induced by the scanner due to the distance between its two rotating mirrors (Navarro and Moreno-Barriuso, 1999). The first mirror changed the horizontal (X) position of the beam, and this resulted on a line scanned on the second mirror, i.e., the object for the second mirror was a horizontal line. The theoretical astigmatism (Moreno-Barriuso, 2000) induced due to the distance between the mirrors of the scanner, d=4.9 mm, depended also on the focal length of the collimating lens used, f'=50.8 mm, and in this case was:

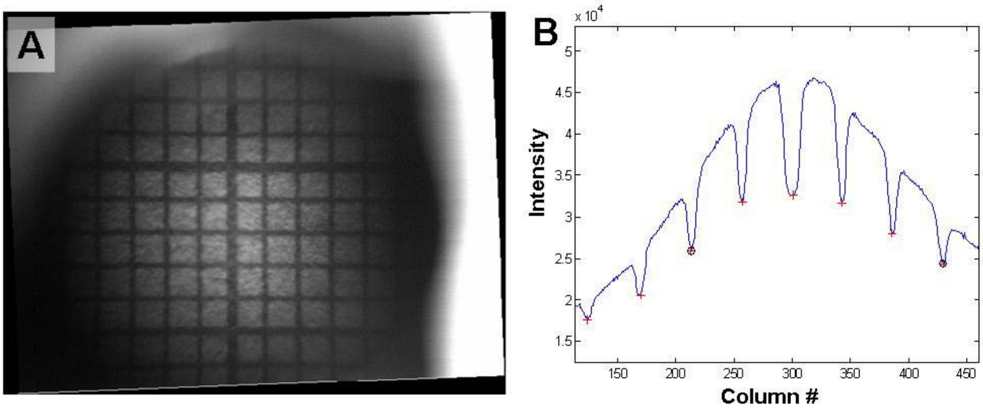

Figure 2.10. Illustration of the Pupil Camera Calibration process: (A) Image of a grid used for the calibration, after rotation. (B) Profile of the image intensity integrated across rows. Crosses indicate local minima, and circles indicate the points used to measure the distance.

$$Ast\ scanner = \frac{d}{\left(f'+d/2\right)\left(f'-d/2\right)} = 1.88D \qquad (2.2)$$

Some astigmatism could also be introduced by other elements of the setup, such as lenses not completely perpendicular to the optical axis.

(a) Astigmatism compensation

As the major contributor to the astigmatism in the system was the scanner (Navarro and Moreno-Barriuso, 1999) a cylindrical trial lens was placed right after the collimation lens of the scanner, with its axis perpendicular to the line joining the mirrors of the scanner (axis at 0^o). To estimate the power of the cylindrical lens experimentally a paper screen was placed on the focal plane of lens L2. This position was found experimentally by slightly changing the location of the screen until the image scanned by the measurement laser spot was a line, as previously mentioned. With this configuration, cylindrical trial lenses of different powers were tested until the lens (+2.50 D at 0^o) that minimised the astigmatism was found. With this lens, the spot appeared static on the retinal plane during the scanning, once defocus was corrected, indicating that the astigmatism was corrected and that the system did not include other significant aberrations.

(b) Scanner calibration

Scanner offset and slope were set up by Carlos Dorronsoro. The offset was chosen to obtain a laser beam aligned with the optical axis of the setup when coordinates (0,0) were selected. Regarding the slope, or ratio scanner voltage/laser displacement, it was selected to obtain the displacement of the laser spot necessary to obtain the desired pattern. For this purpose, a screen with a square grid pattern (1 mm squares) was placed at the pupil plane with the shutter open to see both the spot and the grid. The ratio scanner voltage/laser displacement was calculated as one tenth of the voltage needed to move 10 mm the laser spot impacting on the screen (as observed by the camera) and taking the grid as a reference. After this calibration, most of the astigmatism introduced by the system was compensated. The residual astigmatism was then estimated by measuring the aberrations of an artificial eye consisting of an achromatic doublet of f′=200 mm and a screen acting as a "retina" placed on a sliding support that could be displaced to change the defocus of the eye. Therefore, this artificial eye may be considered nominally unaberrated. The value of the astigmatism was computed from the coefficients Z_2^{-2} and Z_2^{2} (oblique and perpendicular astigmatism, respectively) using the equation:

$$Astigmatism(D) = \frac{4\sqrt{\left(Z_2^{-2}\sqrt{6}\right)^2 + \left(Z_2^{2}\sqrt{6}\right)^2}}{R_{pupil}} \qquad (2.3),$$

where R_{pupil} is the radius of the measured pupil. The value obtained was 0.18±0.03 D (mean ± std across 5 measurements). This value was subtracted from the astigmatism obtained in the measurements.

2.3.4.- SAMPLING PATTERN VERIFICATION

Once the astigmatism of the system was compensated and the scanner calibrated, verification of correct delivering of the sampling pattern selected on the pupil plane was made. To verify this objectively, a paper screen was placed at the pupil plane and captured the images of the spot reflected on the screen for each sample position during a typical run. These images were processed by fitting the spot to a 2-dimensional Gaussian function, with different widths for X and Y axis (because of the asymmetry of the IR laser spot due to astigmatism produced by the laser cavity). In this way the coordinates of the spot position are obtained as the coordinates of the peak, and the spot size in each direction as the corresponding half-width position of the fitted Gaussian function. Figure 2.11 A shows the peak position (red cross) and the position of the half-width on the X and Y axis (blue asterisk) of the fitted Gaussian function superimposed to the image of the corresponding spot. Figure 2.11 B shows a comparison of the nominal sampling positions (black Xs) and those obtained experimentally (red asterisks); error bars indicate the size of the spot in X and Y directions. The largest difference between nominal and experimental coordinates was 0.18 mm, and the mean value (±std) across all 37 spot positions was 0.05 (±0.04) mm; 0.08 (±0.05) mm and 0.03 (±0.02) mm across X and Y coordinates, respectively. It should be noted that these differences are smaller than those found for some of our subjects due to their eye movements, and which were below the variability of the measurement (see Chapter 5, section 5.5.1). Same as described in section 2.2.2.3.-, the wave aberration maps obtained with the nominal and the actual (experimentally obtained) coordinates were compared using aberration data corresponding to one of the human eyes studied in Chapter 5 in order to confirm that these differences (some of which can be attributed to the image capture and processing algorithm) did not affect significantly the estimation of aberrations in real eyes. As can be seen in Figure 2.10 C, the differences between the wave aberration maps obtained from nominal (left) and actual experimental (right) coordinates for the same eye, are negligible. The RMSs for these wavefronts were 0.49 μm and 0.48 μm, respectively. The RMS of the corresponding difference map was

0.03μm, which is negligible compared to the values obtained for human eyes (see section 5.5.1 of Chapter 5).

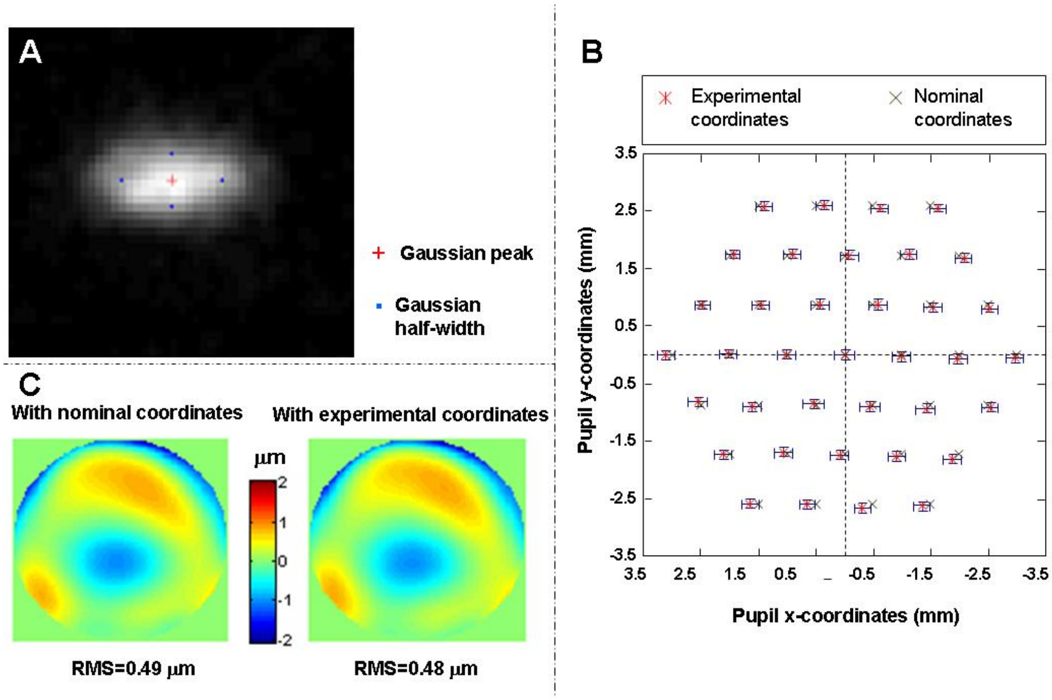

Figure 2.11. Verification of the pupil sampling pattern.

(A) Image of one of the laser spots at the pupil plane. The peak (+) and the half-with (·) positions for the main axes of the fitted Gaussian are superimposed. (B) Nominal (X) and actual (*) positions of the pupil samples. Error bars indicate the size (Gaussian half-width) of the spots in X and Y directions.

The correct delivery of the samples on the pupil plane was crucial to obtain a reliable measurement. Once the correct delivery of the samples on the pupil plane was confirmed, correct identification of the sampling rays with the corresponding retinal aerial images was ensured. For this purpose, the artificial eye described in Section 2.3.3.-(b) was used with the retina displaced closer to the doublet than the focal point in order to make the eye hyperopic. Thus, the spots of the retinal spot diagram will not overlap and no inversion will occur. Then, the correct labelling of the rays in the resulting spot diagram according to the programmed sampling pattern was verified. The spot diagram obtained is shown in Figure 2.12.

Finally, to verify that the processing programme was correct, transverse ray aberrations were computed from the wave aberration (obtained after processing the experimental data) and the corresponding spot diagram positions were verify to coincide with those of the spot diagram obtained experimentally.

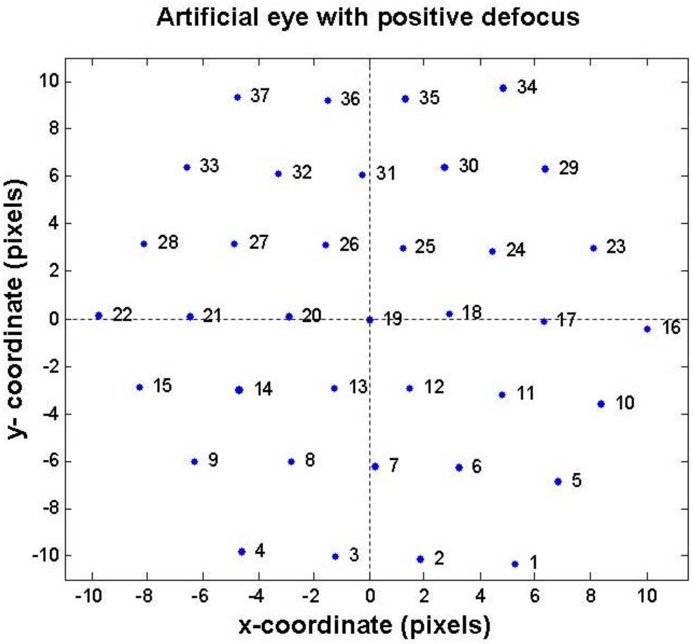

Figure 2.12. Spot diagram corresponding to an artificial eye with positive defocus. The typical sampling pattern used by LRT1 and LRT2 devices to measure aberrations as seen at the retinal plane when positive defocus is present.

2.3.5.- FOCUSING BLOCK SCALE CALCULATION

As explained in section 2.2.1.-, a Badal system was included in the set up to compensate for the subject's refractive error. Figure 2.13 shows the different configurations obtained for different distances between the lenses of the Badal system. For the sake of clarity, the mirrors used to change the distance between the Badal lenses have been removed from the diagram. When the distance between the lenses is equal to the sum of their focal lengths, an afocal configuration is obtained and therefore no correction is induced (see Figure 2.13 A). When the distance between the lenses is longer than the addition of their focal lengths, rays converge towards the eye to compensate hyperopic refractive error (see Figure 2.13 B). When the distance between the lenses is shorter than the sum of their focal lengths, rays diverge towards the eye to compensate myopic refractive error (see Figure 2.13 C).

Since the Badal system in the setup fulfills $f'_1=f'_2=f'$, where f'_1 and f'_2 are the focal lengths of L_1 and L_2, respectively, the Abbe invariant was applied as follows. For L_1: $1/f' = 1/s'_1 - 1/s_1 \Rightarrow s'_1 = f'$, where s_1 and s'_1 are the object and image distances, respectively, for L_1. For L_2: $s_2 = -(f'+d)$ and $1/f' = 1/s'_2 - 1/s_2 \Rightarrow s'_2 = f'(f'+d)/d$, where s_2 and s'_2 are the object and image distances, respectively, for L_2. The distance d_{eye} between the image yielded by L_2 and the position of the eye (at F'_2) is $d_{eye} = s'_2 - f' = f'(f'+d)/d - f' = f'^2/d$, and therefore $D_{eye} = 1000\,d/f'^2$, or:

$$d = \frac{D_{eye}\, f'^2}{1000}, \qquad (2.4)$$

where:

-d is the distance between the L_1 image focus (F'_1) and L_2 object focus (F_2),

- d_{eye} is the distance between the eye (pupil plane) and the position of its far point.

- D_{eye} is the refractive error of the eye.

If the block of two mirrors, or Focusing Block (FB), is moved instead of the lens L_2, to introduce a displacement d in the system the displacement of the mirrors should be $d/2$. Therefore, for a focal length of 100 mm for each Badal lens, the distance d should be 10 mm per dioptre. This means that, in order to induce +1D (i.e., to correct 1 D of hyperopia), the mirrors should be displaced +5 mm. Positive distances indicate the FB moves further away from the eye, and negative distances the opposite.

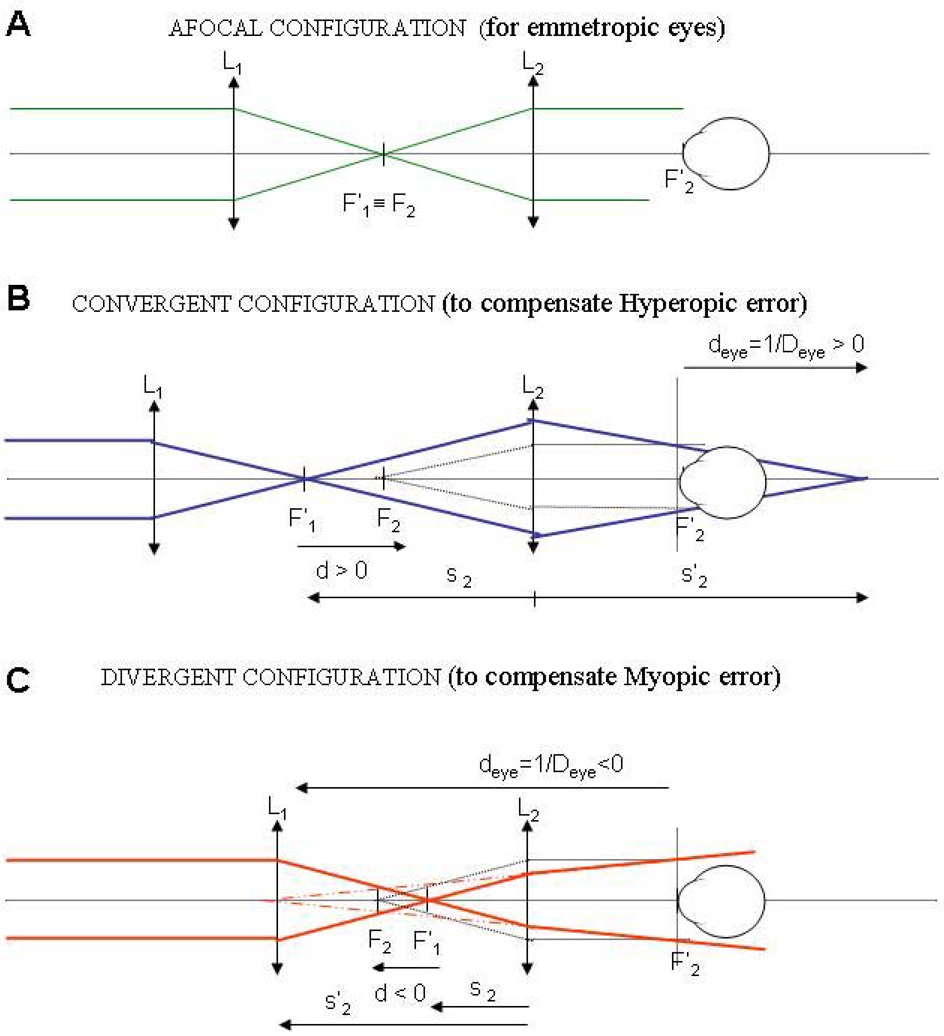

Figure 2.13. Different configurations of the Badal system for refractive error correction. (A) Afocal configuration: distance between the lenses is the sum of their focal lengths, and no correction is induced; (B) When the distance between the lenses is longer than the sum of their focal lengths, and rays converge towards the eye to compensate for hyperopic refractive error; (C) When the distance between the lenses is shorter than the sum of their focal lengths, and rays diverge towards the eye to compensate myopic refractive error.

The position in the setup where 0 D of the FB scale was determined by placing the same nominally non aberrated artificial eye described in Section 2.3.3.-(b) with the screen in its image focal plane (which was found by the autocollimation method) at the pupil plane of the setup. The mirrors were displaced until the scanning spot appeared motionless on the screen of the artificial eye and the retinal camera, and therefore the defocus induced was 0, and that location was marked as 0 Dioptres. The precision in the focusing, computed as the magnitude of the Zernike term for defocus (Z_2^0) in Dioptres, obtained when measuring aberrations with defocus compensated (i.e., the measurement spot was motionless in the retina of the artificial eye while the scanning was on) was -0.05 ± 0.09D (average across 5 measurements ± std).

2.3.6.- COMPENSATION OF DEFOCUS BY THE FOCUSING BLOCK (FB)

In our experimental protocols defocus was systematically corrected using the FB in order to obtain more compact aerial images (and therefore reduce the variability in the processing) and to provide a sharper fixation for the subject. For this reason, a calibration of the defocus compensation by the FB was performed rather than a calibration of the defocus measured by the system. That is, instead of inducing defocus and measuring it, defocus was induced by using trial lenses just in front of an emmetropised (using autocollimation) unaberrated artificial eye (see section 2.3.3.-(b)), and this induced defocus was compensated with the FB. This procedure allowed us to confirm experimentally that the theoretical calculations made in the previous section worked for our system, and that defocus was perfectly compensated by our FB. For this purpose, the scanner was set for continuous scanning so that the green laser beam was constantly moving and turned on the retinal image real time display. Then, for each trial lens, the FB was displaced until the image of the spot in the camera was motionless, indicating that the refractive error induced on the artificial eye by the trial lens had been compensated by the FB. Finally, an aberration measurement was performed in these conditions to verify that the residual defocus after compensation was negligible. This procedure was repeated for different trial lenses (-4D, -3.25 D, -2 D, -1 D, +1 D, +2 D, +3 D, +4 D), obtaining for each lens a value of the FB position in dioptres that compensates for the trial lens power (the same magnitude, with opposite sign would be expected). Figure 2.14 A shows a plot of the nominal compensation by the FB in diopters versus the nominal value of the trial lens (fit: y=-0.98x-0.53; r=0.9996; p<0.0001). As expected, the slope of the fit was practically -1. However, a slight off set was found (-0.53 D). This offset was due mainly to the FB, given that the distance between lenses L1 and L2 of the Badal system for the zero position was slightly shorter than the addition of their focal lengths, and therefore some negative defocus was being introduced in the system.

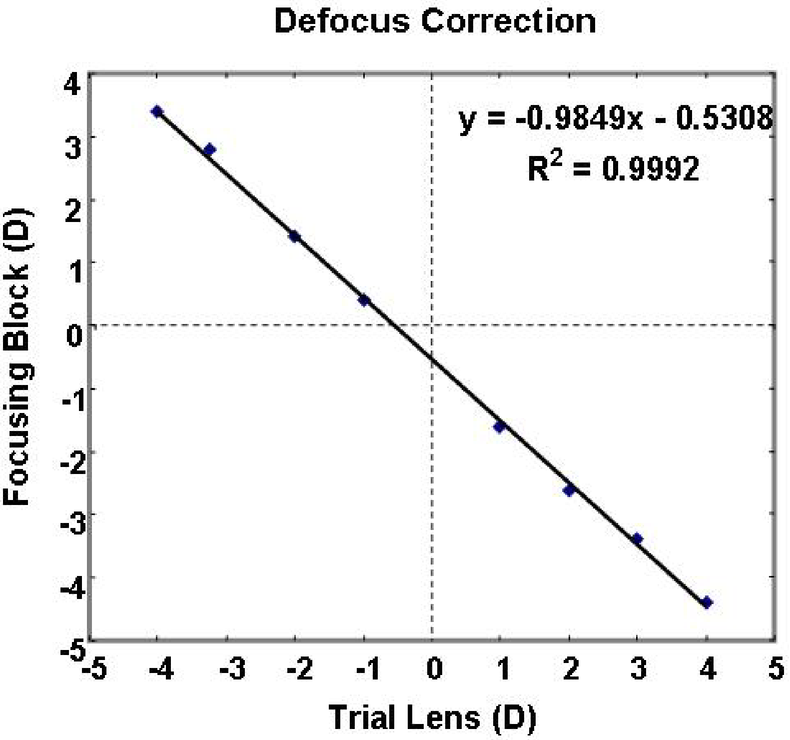

Figure 2.14. Spherical error correction by the Focusing Block versus the nominal value of the trial lens, with the corresponding regression line and equation. The correlation was statistically significant ($p<<0.0001$, $r^2=0.9996$).

For further confirmation, a commercial artificial eye with known defocus was measured, and a residual defocus value similar to the offset found was obtained. However, this small offset in the defocus would not have affected our studies, since refractive error was used in relative terms. In addition, our measurements were performed using IR wavelength and spherical error varies with wavelength as will be described in more detail in Chapter 4. Refraction was also obtained from commercial autorrefractometer or subjective refraction, depending on the study.

Finally, regarding the residual uncorrected defocus accounted for by the aberrations measurement (Z_2^0), the average across the values obtained for the different trial lenses was -0.05±0.09 D. No correlation between the trial lens power and the corresponding residual defocus existed.

2.3.7.- *OPTICAL ABERRATIONS INTRODUCED BY THE SYSTEM*

Before measuring aberrations of human eyes, a verification that neither geometrical nor chromatic aberrations were being introduced by the system was carried out.

(a) Geometrical aberrations

In order to discard that geometrical aberrations were being introduced by the system, the aberrations of the nominally aberration-free artificial eye described in section 2.3.3.-(b) were measured. Table 2.1 shows the RMS values excluding: piston and tilts (2nd through 7th order); and piston, tilts and defocus and astigmatism (3rd through 7th order). Marèchal's criterion (Born and Wolf, 1993), states that an optical system can be considered well corrected in terms of optical aberrations if the RMS departure of the wavefront from the reference sphere is less than $\lambda/14$. In our case, this limit is 0.038 μm and 0.056 μm for λ=532 nm and λ=785 nm, respectively. From the table, the Marèchal's condition fulfils for 3rd and higher order aberrations up to the second decimal. Regarding 2nd order aberrations (defocus and astigmatism), the residual values (see sections 2.3.6.- and 2.3.3.-(b)) will be subtracted to the measured values. Therefore, the system can be considered sufficiently corrected for our purposes.

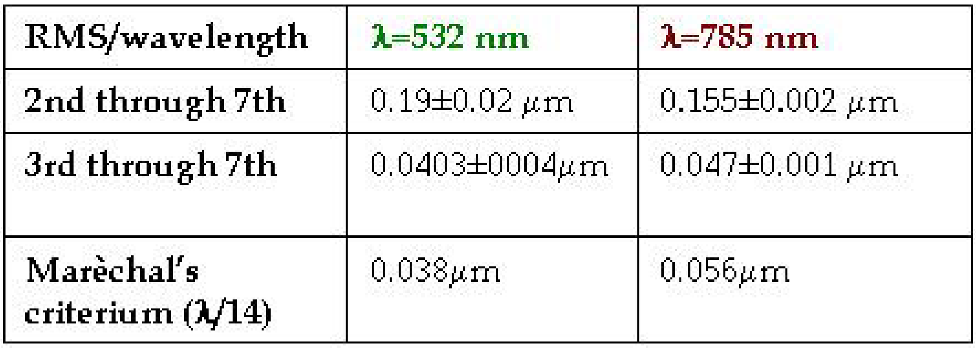

RMS/wavelength	λ=532 nm	λ=785 nm
2nd through 7th	0.19±0.02 μm	0.155±0.002 μm
3rd through 7th	0.0403±0004μm	0.047±0.001 μm
Marèchal's criterium (λ/14)	0.038μm	0.056μm

Table 2.1. RMS values for different orders for the two wavelengths of the setup.

(b) Chromatic aberrations

Absence of chromatic aberration in LRT1 was verified by measuring the aberrations of a phase plate (Navarro et al., 2000) in front of the artificial eye described in Section 2.3.3.-(b), but with a rotating diffuser acting as a retina. The measurements were performed using 543 nm and 786 nm as test wavelengths. The chromatic aberration introduced by the phase plate, which was 12 μm thick, can be considered negligible. The difference in defocus obtained with both wavelengths was 0.04 D.

Similarly, optical aberrations of the artificial eye described in Section 2.3.3.-(b) were measured using IR wavelength (785 nm), under the same conditions (defocus correction, artificial eye position) used for a wavelength of 532 nm. The difference between the values of defocus for both wavelengths was 0.12 D.

2.3.8.- HIGH ORDER ABERRATIONS IN HUMAN EYES

Since two different systems were used in work (particularly, in Chapter 6 both are used simultaneously), confirmation of the equivalence between both systems was required. Also LRT1 had been previously validated with systems from two other independent laboratories, SRR based in a psychophysical technique, in Boston (Moreno-Barriuso et al., 2001a) and a HS sensor in London (Marcos et al., 2002b, Llorente et al., 2003), and therefore the technique, setup and routines to estimate aberrations were independent from ours. Hence, confirmation of the equivalence between both systems also implied a general verification of LRT2.

2.3.8.1.- *LRT1 vs LRT2*

(a) Phase Plate

As a first approach for the comparison of high order aberrations measurement by LRT1 and LRT2 a phase plate with an aberration pattern sculptured using a gray-level single-mask photo-sculpture in photoresist technique (Navarro et al., 2000) was used. This aberration pattern was obtained as the negative of a human eye pattern measured using LRT1. The phase plate was placed in front of the artificial eye described in Section 2.3.3.-(b). The coefficients corresponding to the measurement with LRT1 (dashed blue line) and LRT2 (continuous pink line) are shown on the top graph in Figure 2.15. The corresponding wave aberration maps (left and middle), and difference map (right) are shown on the bottom row. The tendency is very similar when comparing both sets of coefficients and corresponding aberration maps, although the coefficients of LRT2 set are in general larger in absolute value. According to the difference map, differences are concentrated rather in the periphery, near the edges, than in the centre. Although all maps shown in Figure 2.15 have the same diameter, the one corresponding to LRT1 had to be trimmed from 6.5 down to 6 mm. For these reason, some edge effects causing higher aberration values in the edges of the pupil in LRT2 could have been removed from the map corresponding to LRT1. A reliability test was applied to verify the equivalence between the measurements obtained with both systems. For the reliability analysis Cronbach's Alpha model was used, a model of internal consistency usually applied to test scales. The sets of coefficients obtained with the two devices are regarded as scales measuring the same item, and the output of the test, Cronbach's α, indicates the correlation between both scales (1 indicates identity). A value for α as high as 0.94 was obtained, indicating a great correlation. In addition, a significant correlation was found between both measurements (r=0.94, p<0.0001), and no find significant differences were found between the means corresponding to the coefficients obtained with both devices when a Student T-test was applied (p=0.70).

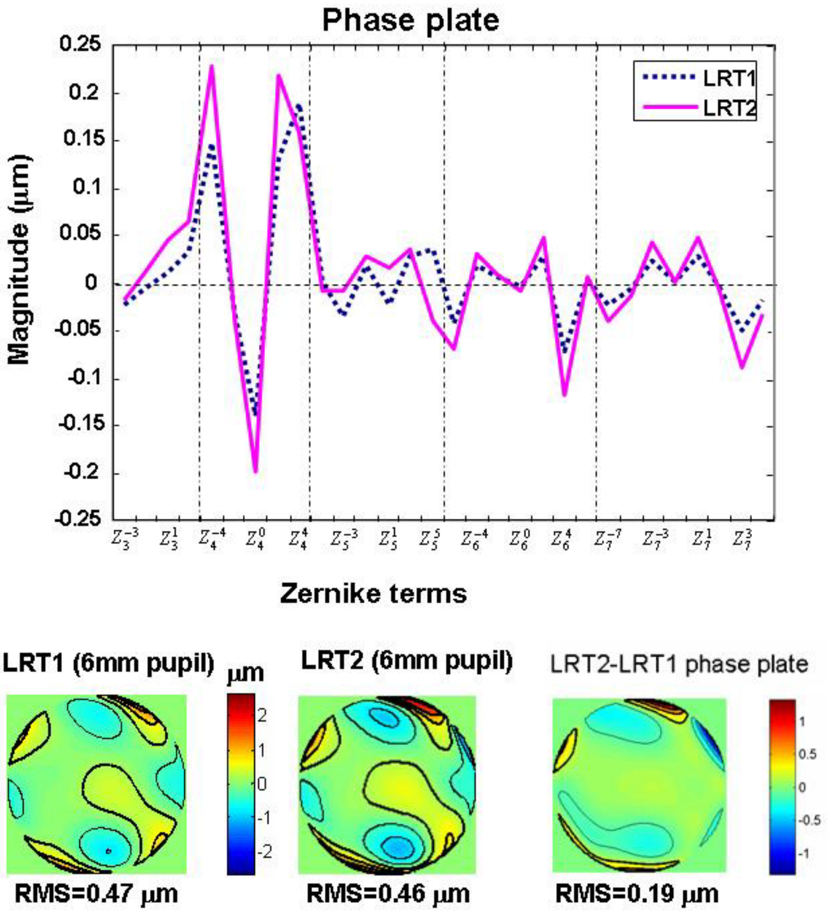

Figure 2.15. Aberrations of the phase plate measured with LRT1 and LRT2. The top graph shows the coefficients obtained with both devices. The wave aberration maps on the bottom row correspond to measurements with LRT1 (left), with LRT2 (middle) and to the difference between the previous two maps (right). Thicker contour lines indicate positive values of the wave aberration.

(b) Human Eyes

To confirm that the system measured higher order aberrations properly in human eyes the measurements obtained for two human eyes from different subjects using both, LRT1 and LRT2 devices were compared. It should be noted that due to the time difference between measurements (51 and 41 months respectively), and the fact that in human eyes the aberration pattern changes with time (Zhu et al., 2004, Mclellan et al., 2001), some differences are expected when comparing aberration patterns. Same as Figure 2.15, Figure 2.16 and Figure 2.17 show average Zernike coefficients (3rd to 7th order) across 4 to 5 runs using LRT1 and LRT2, for eyes #1 and #2 respectively on the top row. Error bars indicate corresponding standard deviation. The similarities between measurements are evident visually when comparing the corresponding wave aberration maps for measurements with LRT1 (left) and LRT2 (middle), and the RMS values (below each map) for both eyes. Also, RMS values corresponding to the difference maps (right) are in the range of the variability of the measurement (0.11±0.04 μm, mean±std RMS of the difference maps from repeated measurements of the eyes studied in Chapter 5, section 5.4.2.2). The reliability test (Cronbach's α model) was applied to the means and standard deviations corresponding to the repeated measurements each device (LRT1 and LRT2), corresponding to each eye. Obtained α values were nearly 1 for the means (0.91 for eye #1 and 0.96 for eye #2), indicating that both devices are measuring practically the same, and slightly lower values for the standard deviations (0.81 for eye #1 and 0.69 for eye #2). When the reliability test was applied to the coefficients corresponding to the repeated measurements obtained with both devices, α was 0.98 for both eyes. A paired Student t-test was applied to verify the correlation between the means and standard deviations of the sets corresponding to each eye, and whether the differences were significant. The measurements with different devices were highly correlated with each other in means ($r=0.84$, $p<0.001$ and r=

0.92, p<0.001, for eyes #1 and #2, respectively) and in standard deviations (r=0.71, p<0.001 and r=0. 69, p<0.001 for eyes #1 and #2, respectively) of the sets. No significant differences were found between the mean set of coefficients corresponding to LRT1 and LRT2 (p=0.449 and p=0.775 for eyes #1 and #2, respectively) for both eyes, and the standard deviations corresponding to the sets of eye #1 (p=0.137), although the standard deviations corresponding to LRT1 and LRT2 were found to be different for eye #2 (p<0.001).

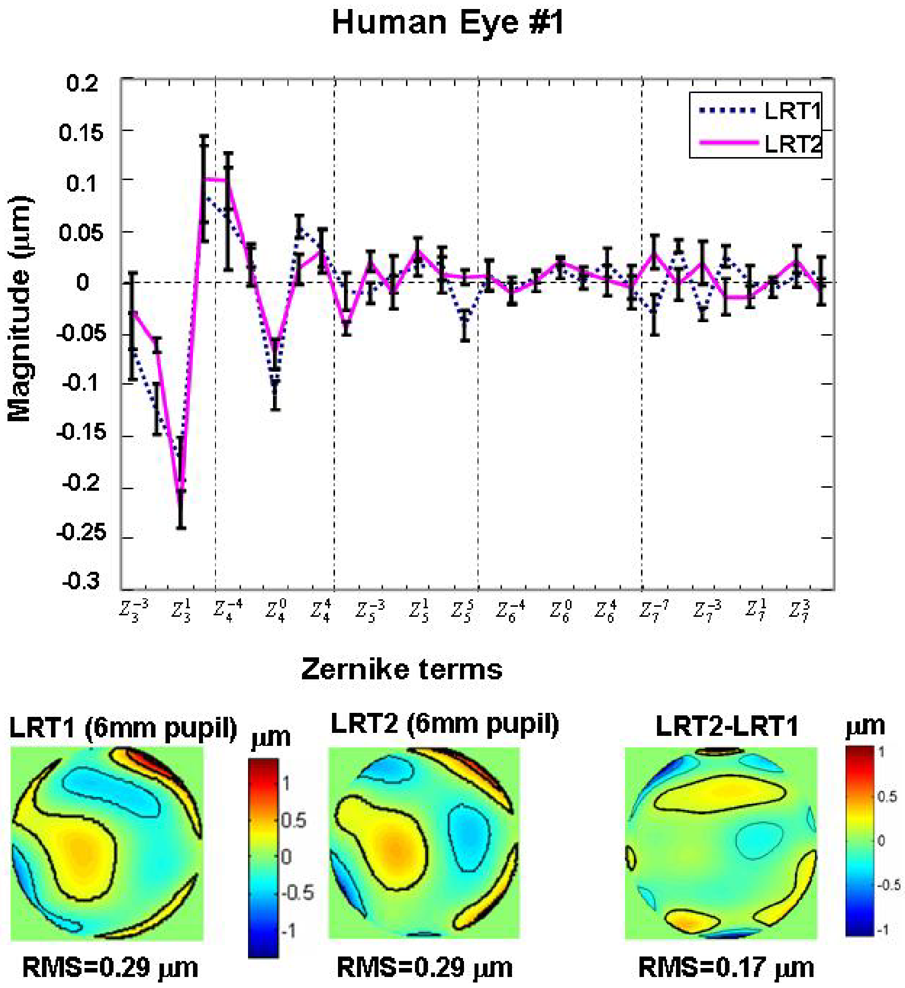

Figure 2.16. Aberrations of Eye #1 measured with LRT1 and LRT2. The top graph shows the average coefficients obtained from 4 to 5 runs with each device. Error bars stand for standard deviation. The wave aberration maps on the bottom row correspond to measurements with LRT1 (left) and LRT2 (middle), and to the difference between these two maps (right). Contour lines are plotted every 0.5 microns. Thicker contour lines indicate positive values of the wave aberration.

A further validation between LRT1 and LRT2 involving human eyes was carried out in the work presented in Chapter 6, where half the eyes were measured with each system. In this validation it was confirmed that the device used to measure ocular aberrations did not have any influence on the results.

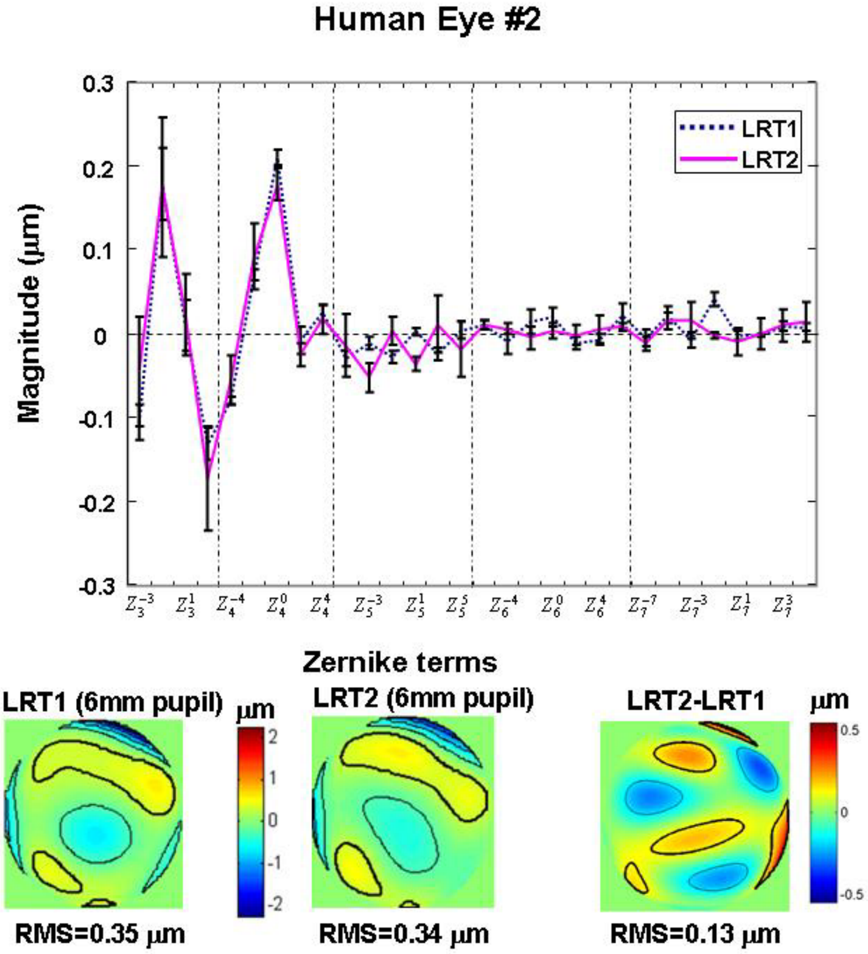

Figure 2.17. Aberrations of Eye #2 measured with LRT1 and LRT2. The top graph shows the average coefficients obtained from four to five runs with both devices. Error bars stand for standard deviation. The wave aberration maps on the bottom row correspond to measurements with LRT1 (left), with LRT2 (middle) and to the difference between the previous two maps (right). Contour lines are plotted every 0.5 microns. Thicker contour lines indicate positive values of the wave aberration.

2.4.- PROTOCOL FOR MEASUREMENTS IN SUBJECTS

Except when specified differently, the protocol used in the measurements with LRT is that described next. The procedures were reviewed and approved by institutional bioethics committees and met the tenets of the Declaration of Helsinki. All patients were fully informed and understood and signed an informed consent before enrolment in the study.

Pupils were dilated with one drop of tropicamide 1% prior to measurement, and the subjects were stabilised by means of a dental impression (LRT1 and LRT2), and a forehead rest. Spherical refractive errors were corrected with spherical lenses (LRT1) or with the Badal system (LRT2) when necessary. As previously mentioned, best focus was assessed by the subject while viewing the fixation stimulus, which was aligned with respect to the optical axis of the system and focused at infinity to keep the subject's accommodation stable during the measurement.

All measurements were done foveally, with a fixation stimulus consisting either on a laser spot corresponding to a 633 nm wavelength He-Ne laser (LRT1) (see Figure 3.1 and Figure 4.1 in chapters 3 and 4, respectively for a diagram of the setup) or a green circle with black radial lines thickening towards the periphery (see fixation test in Figure 2.2 A) (LRT2) and using the centre of the pupil as the reference axis. For proper alignment and continuous monitoring, the pupil was illuminated with IR light and viewed on a CCD centred on the optical axis of the instrument. For LRT2, the pupil was monitored (and recorded) during each run using back-illumination (see section 2.2.1.-), which allowed us to detect issues that would affect the measurements such as tear film break up, blinking or large eye movements. When any of these was detected during a run, the subject was asked to blink a few times until feeling comfortable again, rest or fixate more accurately, respectively, and the measurement was repeated. This was particularly important when sampling patterns with a large number of samples were used (Chapter 5), extending the measurement time.

Each measurement consisted on five runs for each condition to be tested. The pupil sampling pattern used, unless differently specified (Chapter 5), was a hexagonal arrangement of 37 samples which scanned a 6 (LRT2) or 6.5-mm pupil (LRT1). Left and right eyes were analyzed independently for each subject.